

Disorder-controlled relaxation in a 3D Hubbard model quantum simulator

W. Morong^{1,2*}, S.R. Muleady^{3,4*}, I. Kimchi^{3,4}, W. Xu^{1,5},
R.M. Nandkishore^{4,6}, A.M. Rey^{3,4}, and B. DeMarco¹

June 7, 2022

1. Department of Physics, IQIUST, University of Illinois, IL 61801, USA.
2. Present address: Joint Quantum Institute and Joint Center for Quantum Information and Computer Science, University of Maryland and NIST, College Park, Maryland 20742, USA
3. JILA, NIST, Department of Physics, University of Colorado, Boulder, CO 80309, USA
4. Center for Theory of Quantum Matter, University of Colorado, Boulder, CO 80309, USA
5. Present address: Massachusetts Institute of Technology, Department of Physics, Cambridge, MA 02139.
6. Department of Physics, University of Colorado, Boulder, CO 80309, USA.

* These authors contributed equally to this work.

Abstract

Understanding the collective behavior of quantum, many-particle interacting systems is a central problem in modern science. The disordered Fermi-Hubbard model (DFHM) is a key tool for addressing this challenge in the context of strongly correlated electronic solids. This paradigm, which describes interacting particles that tunnel between sites of a crystalline lattice, incorporates disorder to represent the influence of impurities and imperfections on material properties. Tremendous progress has been made on characterizing how disorder and interactions lead to transitions between low-temperature, equilibrium states [1, 2]. However, the extreme complexity associated with out-of-equilibrium behavior, especially in higher dimensions, has made uncovering organizing principles for the dynamical properties of the DFHM model a formidable challenge. Here we show that the relaxation dynamics of doublon excitations (composed of doubly occupied–empty site pairs) [3, 4, 5, 6, 7] in the three-dimensional DFHM model can be understood as a competition between

disorder-enhanced quantum resonances and suppressed diffusive transport. Using interaction-quench measurements on a quantum simulator implemented by cooling fermionic ^{40}K atoms in a cubic optical lattice [8], we find two regimes of doublon decay distinguished by suppression or enhancement of relaxation for increasing disorder. A simple reaction-diffusion model provides an analytical description, which is consistent with the onset of localization for strong disorder. This approach is augmented by developing an approximate numerical technique [9] that shows excellent agreement with the measurements. Our results demonstrate the power of quantum simulators to illuminate the fundamental behavior of complex many-particle quantum dynamics and to provide a pathway for developing computational tools and theoretical understanding, even in regimes that hamper exact solutions [10].

Strong interactions and disorder are known to separately give rise to the celebrated Mott and Anderson metal-insulator transitions [11, 12]. The combined presence of interactions *and* disorder in many physical systems poses the challenge of understanding the interplay between these vastly different localization mechanisms. While progress has been made on theoretically characterizing the equilibrium Mott-Anderson transition at low-temperature [1], many questions still remain, especially regarding time-dependent dynamics far from equilibrium and in higher spatial dimensions.

Dynamics in an interacting quantum many-particle system are generally thought to be suppressed by introducing quenched, or time-independent, disorder. Thermalization can even be entirely prevented by sufficiently strong disorder—a phenomenon known as many-body localization [13, 14, 15, 10]. However, this paradigm is complicated by the formation of quasibound pair-excitations (i.e., doublons) in a clean lattice, leading to an exponential slowing of dynamics for increased interactions [4, 5]. The effect of the interplay between disorder and strong interactions on the dynamics of excitations such as doublons is complex and largely unexplored in experiment and theory.

We study this problem via measurements of doublon relaxation following an interaction quench in a doped, strongly correlated 3D disordered Fermi-Hubbard model (DFHM) (Fig. 1). We find that the relaxation dynamics are captured by a simple reaction-diffusion model, in which the interplay between strong interactions and disorder leads to the presence of quantum resonances throughout the system. This phenomenological picture is further validated by a numerical phase-space technique that can simulate the 3D system and quantitatively reproduce the observed behavior.

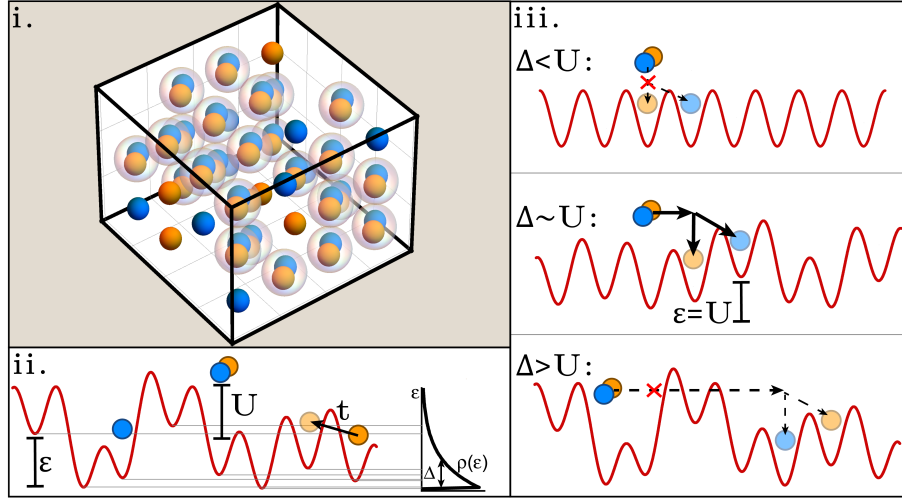


Figure 1: Experimental setup. i: A nonequilibrium doublon population for atoms in two spin states is prepared in a 3D cubic lattice using an interaction quench. ii: The atoms are described by the disordered Fermi-Hubbard model (Eq. 1), which involves tunneling with amplitude t , doublon formation with interaction energy U , and a local disordered energy offset ϵ with an exponential distribution $\rho(\epsilon)$ characterized by disorder strength Δ . iii: For weak disorder (compared to U), the decay of doublons into pairs of single atoms is suppressed by the gap between the doublon and single-particle energies. Moderate disorder can enhance the decay rate by creating resonant pairs of sites with an energy difference comparable to U . However, sufficiently strong disorder can hinder decay by suppressing diffusion to these resonant sites.

Measuring and simulating relaxation

We employ an optical lattice experimental platform (Fig. 1) that was used in previous work [8]. Two spin states (denoted $|\uparrow\rangle$ and $|\downarrow\rangle$) of fermionic ^{40}K atoms are trapped in a cubic lattice superimposed with optical speckle disorder. This system realizes the DFHM with confinement (Fig. 1):

$$H = \sum_{\langle i,j \rangle, \sigma} \left(-t_{ij} \hat{c}_{j\sigma}^\dagger c_{i\sigma} + h.c. \right) + \sum_i U_i n_{i\downarrow} n_{i\uparrow} + \sum_{i,\sigma} \left(\epsilon_i + \frac{1}{2} m \omega^2 r_i^2 \right) n_{i\sigma}. \quad (1)$$

Here, σ indexes the two spin states, t_{ij} is the tunneling energy between sites i and j (restricted to nearest-neighbours, indicated by $\langle i, j \rangle$), U_i is the on-site interaction energy, ϵ_i is the local disordered energy offset, ω is the harmonic confinement, m is the atomic mass, and r_i is the distance of site i from the trap center. The single-particle bandwidth is $12t$ in the absence of disorder. The applied optical speckle field creates disorder in the t , U , and ϵ terms, which have distributions that depend on the overall disorder strength Δ [16, 17]. Because of the harmonic confinement, all measurements are averaged over a density profile that varies from an estimated occupancy $\langle n \rangle = 0.5$ at the center of the trap to zero at the edges of the system.

To probe far-from-equilibrium doublon dynamics, we measure the population of atoms in doubly occupied sites following a quench in which the interactions are reversed from attractive to repulsive using a Feshbach resonance. Before the quench, the gas is in equilibrium with an energetically favorable doublon population. Afterwards, the doublons become excitations that can decay by breaking apart into a pair of single atoms. The atomic doublon population is allowed to evolve in a disordered lattice by turning on the optical speckle field following the interaction quench. After a variable time, the doublon population is measured by mapping each doublon to a tightly bound Feshbach molecule and selectively transferring the $|\downarrow\rangle$ atom in each molecule to an ancillary spin state using an rf sweep (see Methods). Alternatively, we can selectively transfer and image only the single atoms, which allows us to separate doublon decay from overall number loss.

In all regimes, the doublon population decreases following the quench with a rate sensitive to the disorder strength. Typical results at different disorder strengths are shown in Fig. 2. To quantify the decay, we fit the data to a model that describes exponential doublon decay with a time constant τ and that includes overall particle number loss (see Methods). While we find that this fit provides a reasonable characterization of the decay timescale, the functional form of the relaxation is unknown beyond the clean limit. We therefore turn to numerics to provide an interpretation of the timescale with disorder present.

The large scale and dimensionality of our system preclude exact numerical studies and commonly employed approximate techniques, such as DMRG. Therefore, we develop a numerical method—a generalized discrete truncated Wigner approximation (GDTWA)[9, 18, 19]—to simulate the relaxation process. The GDTWA approach invokes a factorization of the density matrix $\hat{\rho}$ of

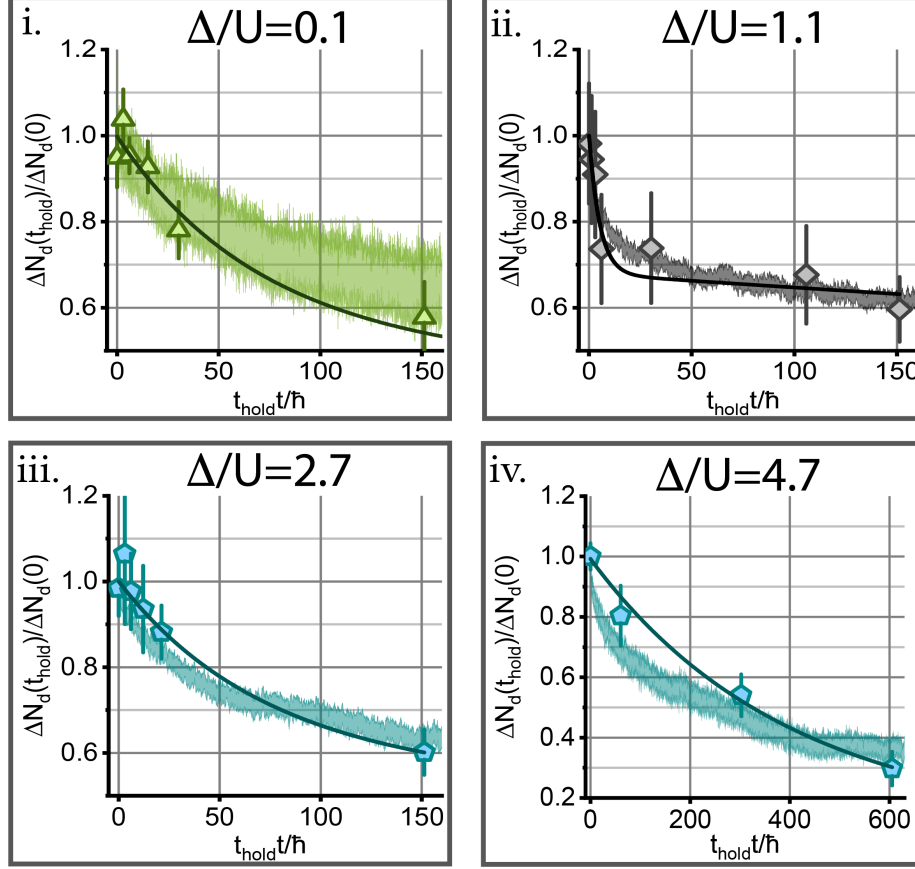


Figure 2: Examples of experimental and numerical doublon relaxation data. Sample traces of the doublon population vs. time for different disorder strengths are shown for experimental measurements (points); the error bars give the statistical standard error of the mean for averaging over multiple measurements. The fits used to extract τ are shown using solid lines. The GDTWA simulation, with an overall scaling and offset (see Methods), is displayed as a shaded region that shows the 95% confidence interval. The horizontal axis for panel iv (the strongest disorder) is compressed to bring the slow decay into view, and all data are taken at $U/12t = 1.8$ (corresponding to a 12 E_R lattice depth in the experiment).

the many-body system over individual lattice sites i : $\hat{\rho} = \bigotimes_i \hat{\rho}_i$. This approximation results in classical equations of motion for tunneling processes between lattice sites, while enabling us to retain full information of the strong on-site Hubbard correlations. The resulting dynamical equations for an initial product state have a trivial mean-field solution. However, we can go beyond this limitation to simulate quantum dynamics by sampling initial configurations from

a semiclassical phase space, thereby introducing a quantum noise distribution and providing a way to capture the buildup of correlations (see Methods).

The GDTWA results, shown as traces in Fig. 2, approximately capture the observed changes in doublon population decay with applied disorder. The GDTWA dynamics also allow us to determine, within the assumptions of the technique, the extent to which τ accurately characterizes the relaxation timescale. We have verified that the non-exponential decay evident in the numerical simulations does not compromise the ability of the fit for τ to correctly capture the decay timescale. Furthermore, we have confirmed that the relaxation timescale is not strongly influenced by density (and the density profile of the gas) in the regime of interest (see Extended Data Figs. 8,9). These tests validate the use of τ to characterize the effects of disorder: the doublon decay is more sensitive to disorder and its interplay with interactions and tunneling compared with other parameters.

Analysis of dynamical regimes

The dependence of τ on disorder is shown in Fig. 3; the qualitative features are shared by experiment and numerics. Strikingly, we find that applying disorder first causes the relaxation time τ to decrease rapidly, before increasing again at higher disorder values. For the clean system, τ is substantially longer than the single-particle tunneling time \hbar/t , which is consistent with previous studies that identified doublons as repulsively bound pairs [3, 4, 5, 6, 7]. However, disorder causes τ to decrease to a minimum value comparable to \hbar/t at a disorder value near $\Delta \sim U/2$. As Δ/U is increased beyond this regime, τ increases, inflating by over two orders of magnitude at the strongest disorder we can apply in the experiment. The separation into two dynamical regimes (distinguished by the slope of τ with Δ) combined with the crossover at $\Delta \sim U$ suggest that the dynamics are controlled by competing mechanisms arising from interactions and disorder.

We can understand these dynamical regimes using a minimal model of diffusing doublons in a disordered environment. In this model, the interchange between doublon-hole pairs and pairs of opposite-spin singly occupied sites is controlled by a set of reaction-diffusion (R-D) equations. The R-D model (see Methods) augments the classical continuum diffusion equation for each particle species with a source term that converts a doublon-hole to a single-single combination, only when the local parameters allow this process to be resonant. In particular, our model requires the local energy difference arising from the speckle disorder to lie within a window of width $\sim t$ around U (see Fig. 1). The doublon diffusion coefficients are taken to decrease monotonically with disorder strength, as increasingly large local energy differences will inhibit doublon transport throughout the lattice.

The R-D model gives the decay rate $1/\tau$ as a product of the effective diffusion rate D_{eff} and the probability P_{reaction} for a conversion between a doublon-hole

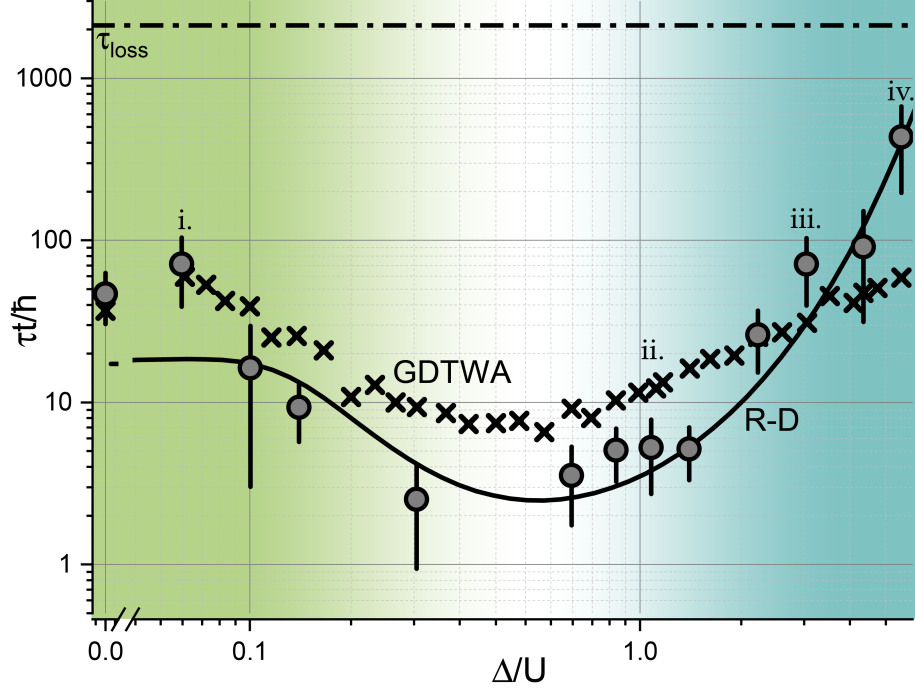


Figure 3: Dynamical regimes of doublon relaxation. The doublon lifetime τ shows a strong non-monotonic dependence on disorder, first decreasing (green region) and then increasing (blue region) with larger disorder strength. The measurements are compared to numerical GDTWA simulations (crosses). The error bars for the experimental data provide the standard error of the fit used to determine τ , while the error bars for the GDTWA numerical data are smaller than the symbols. The solid line represents a fit of the measurements to the analytical reaction-diffusion model with a diffusion constant that decreases monotonically with disorder. The lifetime for atom number loss in the experiment τ_{loss} (dash-dotted line) is independent of disorder and well separated from the doublon dynamics timescale. The labels i.-iv. indicate the values of Δ/U corresponding to panels i.-iv. of Fig. 2.

pair and two singles (\uparrow and \downarrow):

$$1/\tau = P_{\text{reaction}} \times D_{\text{eff}}. \quad (2)$$

The probability of a reaction per site encountered (derived in the Methods) is modeled as

$$P_{\text{reaction}} = p + \exp(-U/\Delta) \sinh(\sqrt{2}zt/\Delta), \quad (3)$$

where p is a small (i.e., of order 0.01) parameter corresponding to reactions in the clean limit, and z is the lattice coordination number. The effective diffusion coefficient D_{eff} gives the rate (linear in time) at which new sites are sampled by any particular doublon. We expect D_{eff} to decrease rapidly with disorder since it is controlled by the doublon diffusion constant. Even in the asymptotically localized phase predicted at large disorder (where doublon diffusion vanishes), D_{eff} should be supplemented by an additional small velocity that allows sampling of sites within the finite localization length.

The exact dependence of diffusion D_{eff} on disorder Δ/U is not qualitatively important as long as D_{eff} decreases monotonically to a very small or vanishing value. In Fig. 3, we choose a diffusion coefficient that decreases exponentially with disorder. We find that an algebraically decaying diffusion coefficient yields quantitatively similar decay rates at all measured disorder strengths. The combined expression for the decay rate $1/\tau$ within this reaction-diffusion model explains the two relaxation regimes as follows.

In regime I ($\Delta \lesssim U$), increasing disorder leads to decreasing decay times. This regime is controlled by the reaction probability P_{reaction} . In the clean limit, the reaction rate is greatly suppressed by the strong interaction energy U , and doublon decay occurs slowly. However, as the disorder strength increases, the tail of the local energy distribution allows for a finite probability of an adjacent site energy difference of order U . By compensating the interaction energy U through this mechanism, the disorder produces a quantum resonance that allows the decay reaction to proceed with high probability, thereby resulting in fast doublon relaxation.

In regime II ($\Delta \gtrsim U$), increasing disorder leads to increasing decay times. This regime is controlled by the diffusion constant D_{eff} , which becomes heavily suppressed by localization effects produced by the large disorder. To a lesser extent, the gradual suppression of the reaction probability due to fewer resonances also contributes to the behavior in this regime. Recent theoretical work suggests that, aside from rare region fluctuations, diffusion should vanish at sufficiently large disorder and signal an asymptotic many-body localized phase [10]. While the experimental data cannot distinguish between $D_{\text{eff}} = 0$ and D_{eff} saturating to a finite small value, we can robustly conclude that diffusion must be highly inhibited in regime II.

Conclusion

Quantum many-body systems involving interactions and disorder can exhibit emergent behavior that, especially in two and three dimensions, is generally

impossible to predict from first principles. By experimentally constructing a DFHM in a 3D optical lattice, we are able to study the dynamical out-of-equilibrium behavior of doublons across vastly different scales of disorder and interactions. Remarkably, we find that constructing a simple model for this extraordinarily complicated system is possible, based on reaction–diffusion equations that are analytically solvable. We devise a numerical approach that captures the same physical effects and shows quantitative agreement with the experiment, supporting our understanding.

Intriguing open questions remain to be explored. In particular, our experimental observations imply a suppression of particle transport as disorder is increased. However, we are unable to distinguish whether this behavior is a manifestation of slow diffusion or a signature of asymptotic many-body localization. Further experiments could help to clarify this difference.

Methods

Experimental procedure.

We use a balanced mixture of the $|F = 9/2, m_F = -9/2\rangle$ and $|9/2, -7/2\rangle$ ^{40}K spin states, which are denoted as $|\uparrow\rangle$ and $|\downarrow\rangle$. The atoms are initially confined in a 1064 nm optical trap with the interactions tuned to be attractive (scattering length $a_s = -75.8 a_0$, where a_0 is the Bohr radius) using the Feshbach resonance near 202.1 G [20]. We load the atoms into a 3D cubic optical lattice with lattice depth $s = 12 E_R$, where $E_R = \hbar^2/(2m\lambda^2)$ is the recoil energy (m is the atomic mass and $\lambda = 782.2$ nm is the lattice wavelength). The state of the gas before the interaction quench is fixed for the data in this study. The quench is realized by increasing the magnetic field by 7 G over 100 μs , after which $a_s = 61.7 a_0$ and $U/12t = 1.8$ (see Extended Data Fig. 6 for data at other interaction strengths). Immediately after the quench, the disorder is turned on over 1 ms with a strength ranging from 0–1.2 E_R . The disorder potential is generated by a 532 nm speckle laser beam created using a holographic diffuser [8, 21]. The disorder ramp rate is chosen to be adiabatic relative to the lattice band gap, but fast compared to the doublon decay rate in the absence of disorder. The rapid turn-on of the disorder may induce disorder-dependent heating of the atoms. We nevertheless can infer that this effect changes the temperature by less than 20% from in-situ measurements of the size of the gas.

After a variable hold time t_{hold} , the lattice potential depth is quickly ramped to 30 E_R to freeze the density distribution, and the disorder is removed by turning off the 532 nm light. The doublon population is measured by ramping the magnetic field across the Feshbach resonance to associate doublons into molecules [22], selectively transferring the $|\downarrow\rangle$ atom in each molecule to the ancillary $|9/2, -5/2\rangle$ state, and imaging only the atoms in the ancillary state. Before imaging, we remove all atoms in the $|\downarrow\rangle$ and $|\uparrow\rangle$ spin states using a combination of rf sweeps and resonant light pulses. Then, the atoms in the ancillary state are transferred to the $|\uparrow\rangle$ state to be imaged on a closed transition.

We extract τ using a fit to a rate model:

$$\dot{N}_d = \dot{N}_{d,neq} + \dot{N}_{d,eq}, \quad (4)$$

$$\dot{N}_{d,neq} = -\frac{1}{\tau}N_{d,neq} - \frac{1}{\tau_{loss}}N_{d,neq}, \quad (5)$$

$$\dot{N}_{d,eq} = -\frac{1}{\tau_{loss}}N_{d,eq}, \quad (6)$$

$$\dot{N}_{s\downarrow} = -\frac{1}{\tau_{loss}}N_{s\downarrow} + \frac{1}{\tau}N_{d,neq}. \quad (7)$$

This model describes a non-equilibrium population of doublons $N_{d,neq}$ that dissociate to create $N_{s\downarrow}$ single $|\downarrow\rangle$ atoms (along with undetected $|\uparrow\rangle$ atoms) at a rate $1/\tau$, a steady-state population of doublons $N_{d,eq}$, and overall number loss at rate $1/\tau_{loss}$. For the longest doublon lifetimes sampled in this work, we perform a simultaneous fit to the changes in the doublon and singles populations to extract τ , while for the shorter lifetimes we find that the singles provide no additional constraint. Measurements used to determine τ_{loss} are shown in Extended Data Fig. 4. The fit values for $N_{d,eq}$ are shown in Extended Data 5, scaled by the initial total atom number (in one spin state) and corrected for the unequal imaging efficiencies of doublons and singles.

Generalized Discrete Truncated Wigner Approximation.

To numerically simulate doublon dynamics, we adapt the generalized discrete truncated Wigner approximation (GDTWA) to our system [9]. We begin by choosing a tensor product structure for the Hilbert space; for the DFHM, we let each subspace correspond to the four-dimensional Hilbert space for each lattice site with basis $\{|\uparrow\downarrow\rangle, |\uparrow\rangle, |\downarrow\rangle, |0\rangle\}$. We then invoke a factorization of the density matrix as a function of time, $\hat{\rho}(t)$, along this tensor product structure, resulting in

$$\hat{\rho}(t) = \bigotimes_j \hat{\rho}_j(t). \quad (8)$$

This approach allows us to retain information regarding the strong on-site correlations between spin species responsible for doublon formation, while treating tunneling induced correlations between sites in a semiclassical manner. However, this method also implicitly invokes a replacement of the anti-commuting fermionic operators with commuting hardcore boson operators. Nonetheless, we expect this to be a good approximation, given that the doublon population relaxation dynamics are expected to be highly insensitive to quantum statistics in the dilute regime explored in the experiment.

The factorization approximation directly results in a set of mean-field-like equations for variables $\lambda_j^\alpha(t) \equiv \langle \hat{\Lambda}_j^\alpha(t) \rangle$, where the Hermitian operators $\hat{\Lambda}_j^\alpha$ correspond to the set of generalized Gell-Mann matrices (GGM) for SU(4) (along with the identity matrix) with index α for each lattice site j , which form a

complete orthonormal basis under a Hilbert-Schmidt norm for the observables on j . The resulting mean-field equations are given by:

$$\frac{d\lambda_j^\alpha}{dt} = i \left[\sum_{\beta} M_j^{\alpha\beta} \lambda_j^\beta(t) + \sum_{\beta, \beta', j'} C_{jj'}^{\alpha\beta\beta'} \lambda_j^\beta(t) \lambda_{j'}^{\beta'}(t) \right] \quad (9)$$

where $M_j^{\alpha\beta} = \text{Tr} [\hat{\Lambda}_j^\beta [\hat{H}_j, \hat{\Lambda}_j^\alpha]]$ and $C_{jj'}^{\alpha\beta\beta'} = \text{Tr} [\hat{\Lambda}_j^\beta \hat{\Lambda}_{j'}^{\beta'} [\hat{H}_{jj'}, \hat{\Lambda}_j^\alpha]]$ for a generic Hamiltonian written as $\hat{H} = \sum_j \hat{H}_j + \sum_{jj'} \hat{H}_{jj'}$. We use the equations arising from this approximation (which lead to trivial mean-field dynamics) to dynamically evolve multiple trajectories randomly sampled from a phase space [9], with a sampling distribution determined by the initial product state of the system. Specifically, if each observable basis element has eigendecomposition $\hat{\Lambda}_j^\alpha = \sum_a \lambda_j^{\alpha,[a]} \hat{P}_j^{\alpha,[a]}$ for eigenvalue $\lambda_j^{\alpha,[a]}$ and corresponding eigenspace projector $\hat{P}_j^{\alpha,[a]}$, then for each trajectory we set $\lambda_j^\alpha(0) = \lambda_j^{\alpha,[a]}$ with probability $p_j^\alpha(a) = \text{Tr} [\hat{\rho}_j(0) \hat{P}_j^{\alpha,[a]}]$.

As we are interested in only the total doublon population, we let each sampled trajectory correspond to a different quenched disorder realization and a different random initial product state configuration respecting the lattice filling (see comparisons with exact results in Extended Data Fig. 7). Each dynamical curve in Fig. 2 results from averaging 1,000 such trajectories in a $4 \times 4 \times 4$ lattice with periodic boundary conditions, with a fixed but randomly distributed initial loadout of seven doublons and 12 singly occupied sites, or singles, of each spin flavor. In benchmarking, we have generally found that the resulting decay times are robust to increases in the system size and variations in the single density (see Fig. 8). The insensitivity to density enables comparison with the experiment despite the variation in single density across the trap.

In contrast to the decay time, the steady-state doublon fraction is strongly dependent on the single density. Since we are only interested in the decay time, we linearly rescale the simulation results for the doublon population to make a visual comparison with the experiment (i.e., $N_d(t) \rightarrow a \times N_d(t) + b$). This procedure amounts to taking the initial and final doublon populations as free parameters for a weighted least-squares fit to the experimental decay data. Additionally, we multiply the simulation results by a phenomenological particle loss factor using the measured loss rate when comparing to the experiment (see Fig. 2).

In our simulations, we neglect the relatively small disorder in the tunnelling and interaction parameters. We also ignore the presence of the harmonic confining trap: assuming diffusive motion, the doublons in the trap center will not travel an appreciable distance towards resonant regions in the trap edges before decaying. We expect both of these features to result in small shifts to the effective disorder strength and diffusion coefficients, but not to affect the main features of our results.

The simulations reveal several non-exponential features of the decay dynamics. In order to extract consistent decay times, we perform two different fitting methods on the simulation data. The first method is optimized to accurately capture the initial decay of the numerical data, while the second is optimized for comparison to the experiment. In the first method (displayed in Fig. 2), we fit the dynamical curves to an exponential decay with a nonzero steady-state, and we constrain this function to start at the exact initial doublon number. This technique allows us to capture the rapid early time decay dynamics (see Fig. 2). An unconstrained fit virtually ignores the early time regime and is more heavily influenced by the long period of slow, exponential relaxation at late times, leading to a significant underestimate of the decay time and initial doublon number. In the second method, which is displayed in Extended Data Fig. 9, we only use simulation data at times corresponding to the experimental measurements. This latter method takes into account experimental bias from the selected hold times, thus providing a consistency check between simulation and experiment. This technique produces generally better quantitative agreement in the crossover regime.

Reaction-Diffusion Model.

In this model, we let each particle species obey a R-D equation, e.g. for the doublon number $n_d(\mathbf{r}, t)$, as a function of space \mathbf{r} and time t ,

$$\partial_t n_d = D_d \nabla^2 n_d + S(\mathbf{r})(n_{s\uparrow} n_{s\downarrow} - n_d n_h). \quad (10)$$

The source term $S(\mathbf{r})$ has contributions from quantum fluctuations and disorder. Here we focus on the latter contribution, relevant when disorder is not too small. $S(\mathbf{r})$ is modeled by a small constant clean-system reaction probability p , together with a Boolean step function signifying resonance with local energy difference $\mu(\mathbf{r})$,

$$S(\mathbf{r}) = p + \Theta(\gamma - |\mu(\mathbf{r}) - U|) \quad (11)$$

where γ is the width of the resonance and $\mu(\mathbf{r})$ is the difference of two independent random local energies from the speckle distribution,

$$\wp(\mu) = \frac{1}{2\Delta} \exp(-|\mu|/\Delta). \quad (12)$$

The resulting $S(\mathbf{r})$ distribution yields a reaction ($S \approx 1$) with probability

$$P(\{S = 1\}) = p + \int_{U-\gamma}^{U+\gamma} \wp(\mu) d\mu = p + \exp(-U/\Delta) \sinh(\gamma/\Delta), \quad (13)$$

which is also the average of $S(\mathbf{r})$. We expect $\gamma \approx \sqrt{2}zt$ for lattice coordination number z ($z = 6$ for a cubic lattice in 3D), though the exact form is unimportant for the general conclusions we wish to draw. We also find that the form of $S(\mathbf{r})$ is qualitatively similar to the form obtained by convolving the speckle distribution with a heavy-tailed Lorentzian resonance peak.

To proceed, let us work to linear order in n_d (controlled in the dilute limit) and take $t \ll \Delta$, arriving (with $D = D_d$) at a linear differential equation with an inhomogenous random source term,

$$\partial_t n_d(\mathbf{r}, t) = D \nabla^2 n_d(\mathbf{r}, t) - S(\mathbf{r}) n_d(\mathbf{r}, t). \quad (14)$$

The homogeneous solution to the heat equation of a point particle in $d = z/2$ dimensions is $n(\mathbf{r}, t) = (4\pi Dt)^{-d/2} \exp(-\mathbf{r}^2/4Dt)$. The linear diffusion range grows as $\sqrt{2dDt}$, which is also proportional to the number of sites sampled when $d = 1$. In 3D, however, the number of sites sampled grows linearly in time as $N_S = \alpha Dt$ with $\alpha \approx 1.32$. This yields a decay constant

$$\Gamma = \alpha D(\Delta) \left[p + \exp(-U/\Delta) \sinh\left(\sqrt{2}zt/\Delta\right) \right]. \quad (15)$$

For a diffusion constant of the form $D(\Delta) = D_0 \exp(-\Delta/\Delta_0)$, we fit the model to the experimental data with unknowns p , D_0 , and Δ_0 , resulting in the line shown in Fig. 3. The best fit parameters are $p = 0.011 \pm 0.007$, $\hbar D_0/t = 4 \pm 1$, and $\Delta_0/U = 0.88 \pm 0.09$.

Data Availability

The data and code that support the findings of this study are available from the corresponding author upon reasonable request.

References

- [1] Belitz, D. & Kirkpatrick, T. R. The Anderson-Mott transition. *Rev. Mod. Phys.* **66**, 261–380 (1994).
- [2] Byczuk, K., Hofstetter, W. & Vollhardt, D. Anderson localization vs. Mott–Hubbard metal–insulator transition in disordered, interacting lattice fermion systems. *Int. J. Mod. Phys. B* **24**, 1727–1755 (2010).
- [3] Winkler, K. *et al.* Repulsively bound atom pairs in an optical lattice. *Nature* **441**, 853–856 (2006).
- [4] Strohmaier, N. *et al.* Observation of Elastic Doublon Decay in the Fermi-Hubbard Model. *Phys. Rev. Lett.* **104**, 080401 (2010).
- [5] Sensarma, R. *et al.* Lifetime of double occupancies in the Fermi-Hubbard model. *Phys. Rev. B* **82**, 224302 (2010).
- [6] Hansen, D., Perepelitsky, E. & Shastry, B. S. Split Hubbard bands at low densities. *Phys. Rev. B* **83**, 205134 (2011).
- [7] Covey, J. P. *et al.* Doublon dynamics and polar molecule production in an optical lattice. *Nat. Comm.* **7**, 11279 (2016).

- [8] Kondov, S. S., McGehee, W. R., Xu, W. & DeMarco, B. Disorder-Induced Localization in a Strongly Correlated Atomic Hubbard Gas. *Phys. Rev. Lett.* **114**, 083002 (2015).
- [9] Zhu, B., Rey, A. M. & Schachenmayer, J. A generalized phase space approach for solving quantum spin dynamics. *New. J. Phys.* **21**, 082001 (2019).
- [10] Abanin, D. A., Altman, E., Bloch, I. & Serbyn, M. Colloquium : Many-body localization, thermalization, and entanglement. *Rev. Mod. Phys.* **91**, 021001 (2019).
- [11] Mott, N. F. The Basis of the Electron Theory of Metals, with Special Reference to the Transition Metals. *Proc. Phys. Soc. Sect. A* **62**, 416–422 (1949).
- [12] Anderson, P. W. Absence of Diffusion in Certain Random Lattices. *Phys. Rev.* **109**, 1492–1505 (1958).
- [13] Gornyi, I. V., Mirlin, A. D. & Polyakov, D. G. Interacting electrons in disordered wires: Anderson localization and low-T transport. *Phys. Rev. Lett.* **95**, 206603 (2005).
- [14] Basko, D. M., Aleiner, I. L. & Altshuler, B. L. Metal–insulator transition in a weakly interacting many-electron system with localized single-particle states. *Ann. Phys.* **321**, 1126–1205 (2006).
- [15] Nandkishore, R. & Huse, D. A. Many-Body Localization and Thermalization in Quantum Statistical Mechanics. *Annu. Rev. Condens. Matter Phys.* **6**, 15–38 (2015).
- [16] Zhou, S. Q. & Ceperley, D. M. Construction of localized wave functions for a disordered optical lattice and analysis of the resulting Hubbard model parameters. *Phys. Rev. A* **81**, 013402 (2010).
- [17] White, M. *et al.* Strongly Interacting Bosons in a Disordered Optical Lattice. *Phys. Rev. Lett.* **102**, 055301 (2009).
- [18] Schachenmayer, J., Pikovski, A. & Rey, A. M. Many-Body Quantum Spin Dynamics with Monte Carlo Trajectories on a Discrete Phase Space. *Phys. Rev. X* **5**, 011022 (2015).
- [19] Acevedo, O. L. *et al.* Exploring many-body localization and thermalization using semiclassical methods. *Phys. Rev. A* **96**, 033604 (2017).
- [20] Loftus, T., Regal, C., Ticknor, C., Bohn, J. L. & Jin, D. S. Resonant control of elastic collisions in an optically trapped Fermi gas of atoms. *Phys. Rev. Lett.* **88**, 173201 (2002).

- [21] Kondov, S. S., McGehee, W. R., Zirbel, J. J. & DeMarco, B. Three-Dimensional Anderson Localization of Ultracold Matter. *Science* **334**, 66–68 (2011).
- [22] Jördens, R., Strohmaier, N., Günter, K., Moritz, H. & Esslinger, T. A Mott insulator of fermionic atoms in an optical lattice. *Nature* **455**, 204–207 (2008).

Acknowledgements

We acknowledge helpful discussions with Gretchen Campbell and Jason Iaconis. This work is supported by the AFOSR grant FA9550-18-1-0319; the ARO single investigator award W911NF-19-1-0210; the NSF PHY-1820885 and NSF JILA-PFC PHY-1734006 grants; and NIST. It is also supported in part by the AFOSR under grant number FA9550-17-1-0183 (R.M.N.).

Author Contributions

W.M., W.X., and B.D. conceived the study and contributed to experimental design, data collection, and analysis. S.R.M., I.K., R.M.N., and A.M.R. contributed to development and application of the analytical theory and the numerical simulations. All authors contributed to discussion of the results and to the manuscript.

Competing interests

The authors declare that they have no competing financial interests.

Correspondence and requests for materials should be addressed to B. DeMarco (email: bdemarco@illinois.edu).

Extended Data

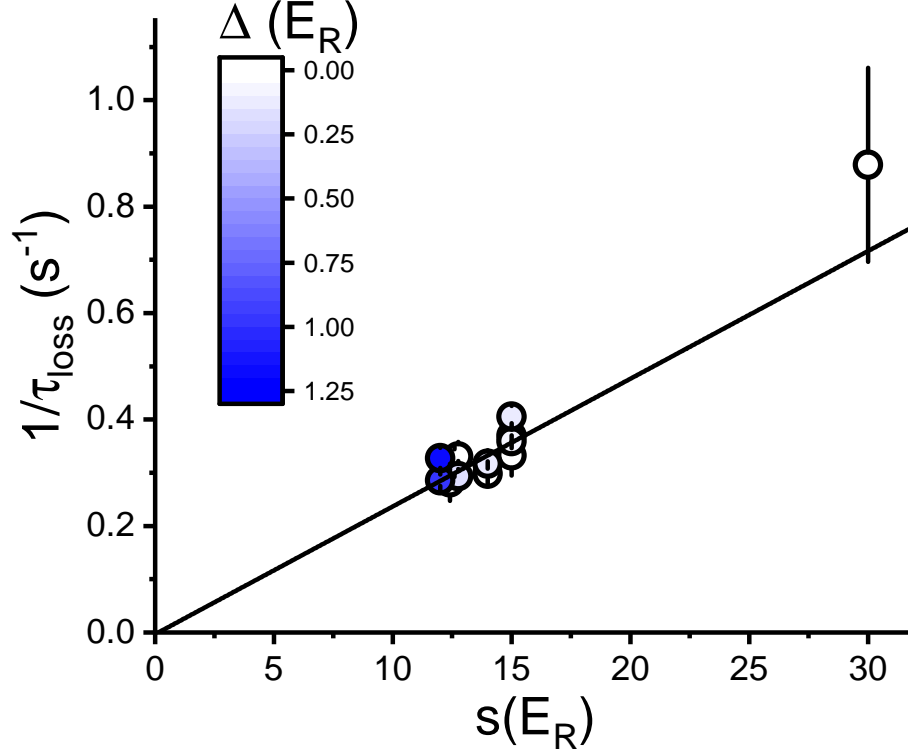


Figure 4: Extended data: Experimental atom number loss rate. The measured loss rate $1/\tau_{\text{loss}}$ is shown for various lattice depths s and disorder strengths. Both the lattice depth and disorder are measured in units of the recoil energy of the lattice (E_R). The loss rate scales linearly with lattice depth and is independent of disorder strength. This behavior is consistent with off-resonant scattering of lattice light as the dominant loss mechanism. The slope of a linear fit (solid line, constrained to have no intercept) is $0.0238 \pm 0.0005 (s \cdot E_R)^{-1}$. We use this fit to determine the value of τ_{loss} used in the fitting model for doublon decay data in which only the doublon population is measured.

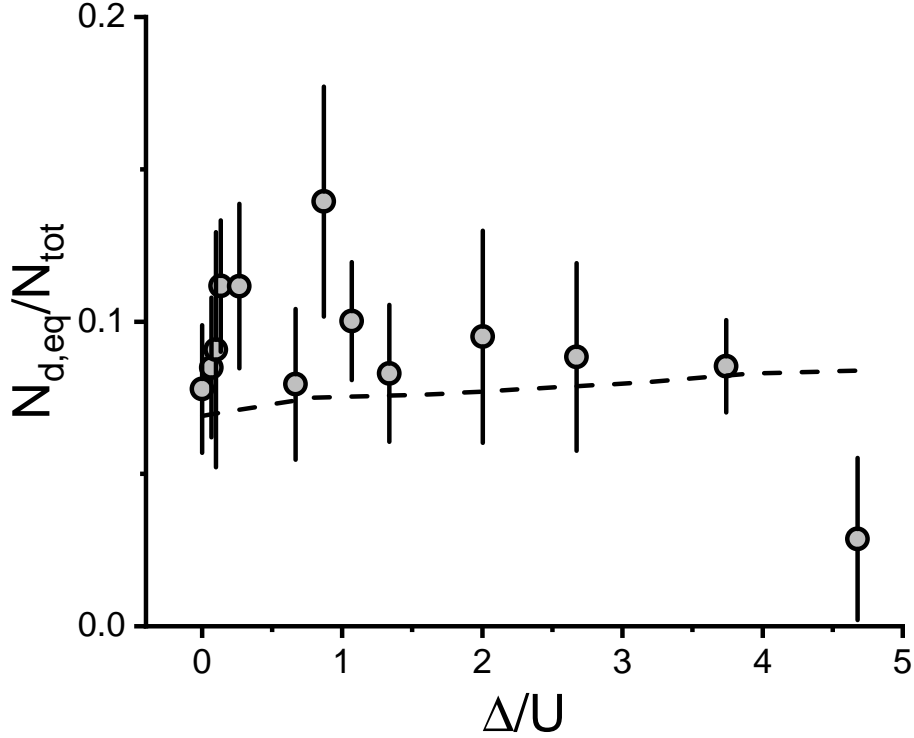


Figure 5: Extended data: Disorder dependence of steady-state doublon fraction, corresponding to the data in Fig. 2. The steady state doublon population $N_{d,eq}$ is extracted from the fits to the doublon decay (see Methods), while the total number in one spin N_{tot} is measured in separate experimental runs. The error bars display the standard error in the fit. To determine the absolute doublon number (and compare with the total atom number), we image the $|\downarrow\rangle$ atoms in singly occupied sites by changing the rf frequency for the sweep during the imaging procedure. By comparing the number that vanish in the doublon population to the corresponding appearance of single atoms, we benchmark the relative detection of doublon vs single atoms at 50%. This inefficiency may arise from inelastic decay of Feshbach molecules during the imaging procedure and imperfect association of doublons into Feshbach molecules. The steady-state value is comparable to the result from an atomic limit calculation at equilibrium (dashed line) that neglects the entropy generated by the quench (which is expected to be substantially smaller than the entropy present from finite temperature). However, the 50% doublon imaging efficiency should be treated as a systematic uncertainty in the doublon number, since we lack a microscopic model for the imaging process.

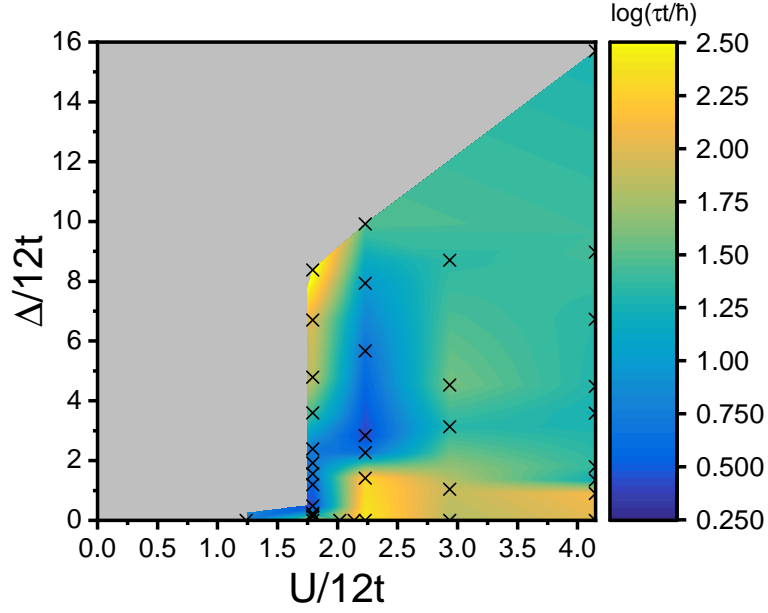


Figure 6: Extended data: Dependence of measured τ on $U/12t$. The lattice depth is tuned from 11–15 E_R to vary $U/12t$ across the range sampled in these data. The crosses represent experimental points, which are interpolated to create the colormap. Stronger interactions generally result in enhancement of slow relaxation at low disorder and recession of slow relaxation at high disorder. For the strongest interactions ($U/12t = 2.9, 4.2$), the measured lifetime in the clean limit is likely limited by technical imperfections; the predicted elastic doublon decay lifetimes for these points (using the scaling of Ref. [4], which is consistent with our measurements at lower $U/12t$) are one and nine seconds, respectively.

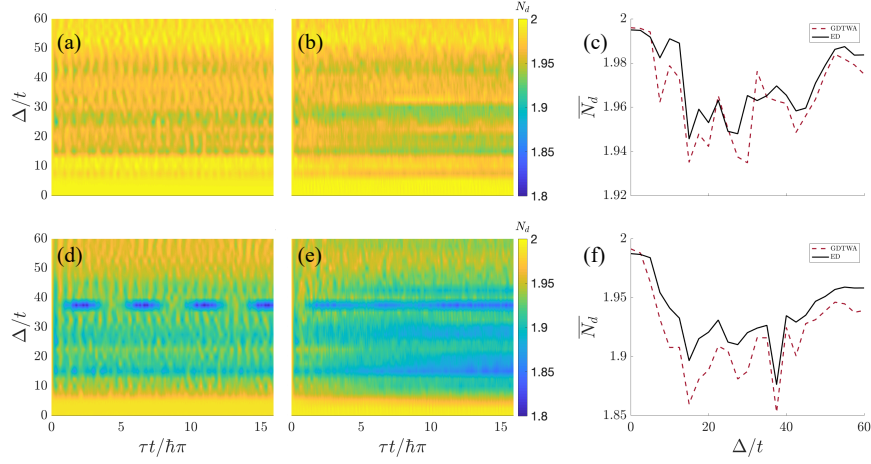


Figure 7: Extended data: GDTWA benchmarking in 1D. A comparison of the total doublon number dynamics obtained from exact diagonalization of the DFHM(a,d) and GDTWA (b,e) is shown, as described in the Methods, for a periodic 1D chain of eight lattice sites. These simulations were carried out with $U/12t = 2.5$, and the results were averaged over 100 disorder realizations for each disorder strength. The top row (a-c) corresponds to an initial loadout of two doublons and no singles, while the bottom row (d-f) corresponds to an initial loadout of two doublons and one single of each flavor. Panels (c) and (f) give the doublon population time-averaged over the last half of the time interval shown. For system sizes accessible by exact simulation, the initial doublon population quickly jumps to the steady state, without any further relaxation features observable on longer timescales.

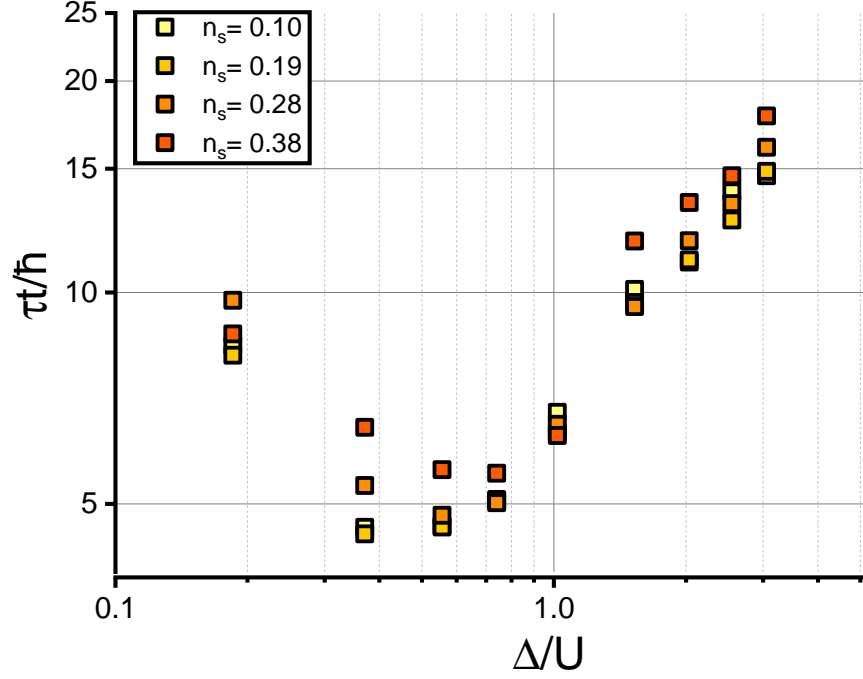


Figure 8: Extended data: GDTWA variation of decay times with single density. A comparison of GDTWA decay times at selected values of Δ/U for a $6 \times 6 \times 6$ lattice with different initial single densities. These results were averaged over 50 disorder/initial configuration realizations, with each configuration also averaged over 50 GDTWA trajectories. Here, $U/12t = 1.8$, and the initial doublon density remains fixed at 11%. While the steady-state population depends strongly on the initial single density, the robustness of the decay time to this parameter allows comparison with experiment, despite the spatially varying density in the trap.

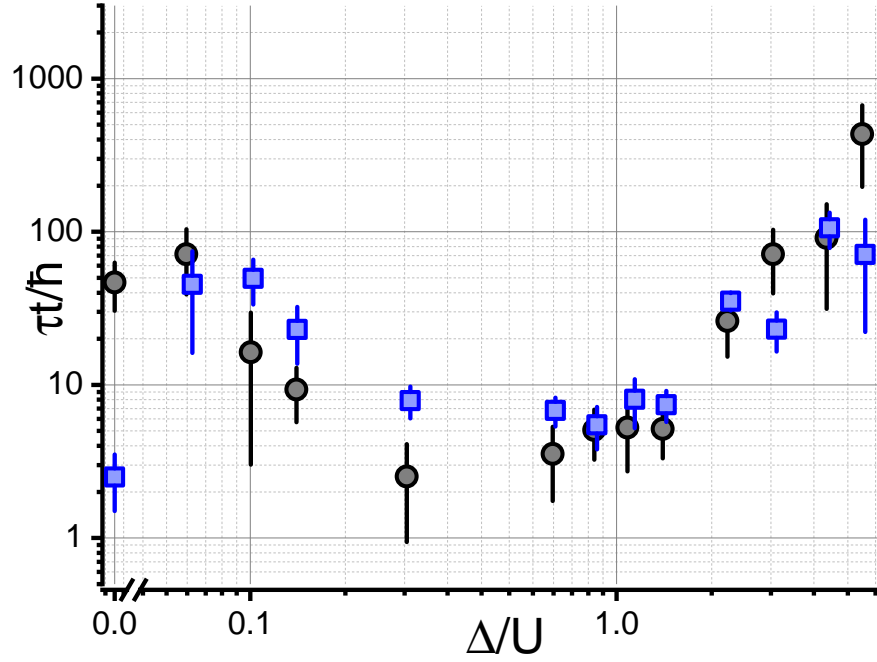


Figure 9: Extended data: GDTWA relaxation times from biased fits. A comparison between experimental (black circles) and GDTWA decay times (blue squares) is shown. The GDTWA decay times are extracted utilizing a (disorder-dependent) sampling function consisting of delta peaks at the experimental hold times, weighted by the appropriate experimental uncertainty. The error bars show the fit standard error, obtained from a linearized curvature analysis.